Energetic Chromophores: Low-Energy Laser Initiation in Explosive Fe(II) Tetrazine Complexes

Thomas W. Myers,[*,†] Josiah A. Bjorgaard,[‡] Kathryn E. Brown,[§] David E. Chavez,[†] Susan K. Hanson,[‖] R. Jason Scharff,[†] Sergei Tretiak,[‡] and Jacqueline M. Veauthier[‖]

[†]M Division, [‡]Theoretical Division, [§]W Division, and [‖]Chemistry Division, Los Alamos National Laboratory, P.O. Box 1663, Los Alamos, New Mexico 87545, United States

S *Supporting Information*

ABSTRACT: The synthesis and characterization of air stable Fe(II) coordination complexes with tetrazine and triazolo-tetrazine ligands and perchlorate counteranions have been achieved. Time-dependent density functional theory (TD-DFT) was used to model the structural, electrochemical, and optical properties of these materials. These compounds are secondary explosives that can be initiated with Nd:YAG laser light at lower energy thresholds than those of PETN. Furthermore, these Fe(II) tetrazine complexes have significantly lower sensitivity than PETN toward mechanical stimuli such as impact and friction. The lower threshold for laser initiation was achieved by altering the electronic properties of the ligand scaffold to tune the metal ligand charge transfer (MLCT) bands of these

materials from the visible into the near-infrared region of the electromagnetic spectrum. Unprecedented decrease in both the laser initiation threshold and the mechanical sensitivity makes these materials the first explosives that are both safer to handle and easier to initiate than PETN with NIR lasers.
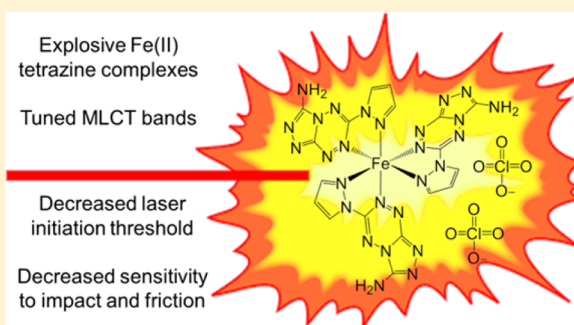
■ INTRODUCTION

Laser initiation of explosives is a safer and more reliable alternative to conventional mechanical or electrical initiation methods. Recent work using near-infrared (NIR) lasers has shown promise, but progress in this area has been limited by the lack of suitable materials that are both safe and have acceptable laser initiation thresholds.[1] Primary explosives such as lead azide can be laser initiated at low laser energy densities[2,3] but are by definition highly susceptible to accidental initiation because of their high sensitivity to mechanical stimuli (e.g., impact, friction). Indeed, lead azide is the explosive with the lowest reported threshold for laser initiation (11 mJ/cm^2 at 1064 nm).[3] Primary explosives that are less sensitive than lead azide such as those recently reported by the Klapötke group can also be initiated with NIR diode lasers but at energy densities 3 orders of magnitude greater than that of lead azide (6.5−10 J/cm^2 at 940 nm).[4,5]

To our knowledge, the only single component secondary explosive that has been initiated with NIR light is PETN (PETN = pentaerythitol tetranitrate), which has a threshold of 21 J/cm^2 (at 1064 nm).[6] The initiation threshold of PETN at 1064 nm can be reduced to 6.4 J/cm^2 by decreasing the density of the PETN powder; however, this lowering of the density consequently increases the sensitivity of PETN toward mechanical stimuli. Overall, the strong correlation between lower mechanical sensitivity and higher initiation thresholds has prevented improvements in both safety and reliability in laser initiation systems.

One way to try to break this trend is to match the absorption of the explosive material to the wavelength of the laser. PETN absorbs ultraviolet (UV) light but does not absorb significant amounts of visible or NIR light.[7] Although UV lasers are not practical for laser initiation, utilizing UV light in place of NIR light for the initiation of low-density PETN leads to a decrease of the threshold to 2.5 J/cm^2 (at 266 nm). Improvements to the initiation threshold at NIR wavelengths (1.4 J/cm^2, 1064 nm) have been achieved through doping nonexplosive absorbent material into PETN.[8] However, the presence of nonexplosive dopants can alter both the explosive performance and the sensitivity properties of these materials. If a pure explosive material with significant absorptions of NIR light can be synthesized, then further improvements in both safety and reliability should be achievable.

Metal coordination complexes with tetrazine ligands have the potential to be highly absorbent secondary explosives. Tetrazines display rich spectroscopic properties both as pure organic compounds[9] and as ligands in coordination complexes.[10] In addition, these nitrogen-rich tetrazine moieties can be incorporated into explosives without compromising densities, mechanical sensitivities, or performance properties.[11] It has been demonstrated that coordination of tetrazine ligands with Cu(I) or Fe(II) metal centers yields complexes with intense metal-to-ligand charge transfer (MLCT) bands in the

visible regions of the electromagnetic spectrum.[12] Additionally, we have demonstrated that these intense MLCT bands are maintained in explosive metal tetrazine complexes.[13] Although these initial energetic tetrazine coordination complexes were secondary explosives, they were not suitable for initiation experiments because they did not absorb NIR light.

Herein we report the synthesis and characterization of explosive Fe(II) complexes with nitrogen-rich tetrazine and triazolo-tetrazine ligands. We also provide time-dependent density functional theory (TD-DFT) modeling of these systems to explain and predict how changes to the electronic structure of the ligands shift the MLCT bands from the visible to the NIR region of the spectrum. Through this work, we seek to break the observed trend between low mechanical sensitivity and high initiation thresholds to develop the first single-component secondary explosive candidates for NIR optical initiation systems.

■ RESULTS AND DISCUSSION

Synthesis. We have previously reported the synthesis of energetic complexes of 3-amino-6-(3,5-dimethylpyrazolyl)-1,2,4,5-tetrazine (NH$_2$TzDMP, 3) with Fe(II) metal centers.[13] The complexes were limited to absorption of visible light and had poor oxygen balance. To tune the MLCT band to lower energies, we selected ligands with the 1,2,4-triazolo[4,3-b]-[1,2,4,5]-tetrazine fused ring system in addition to ligands based on our initial 1,2,4,5-tetrazine ring system(Scheme 1).

**Scheme 1. Synthesis of 3−10 from 1 and 2**
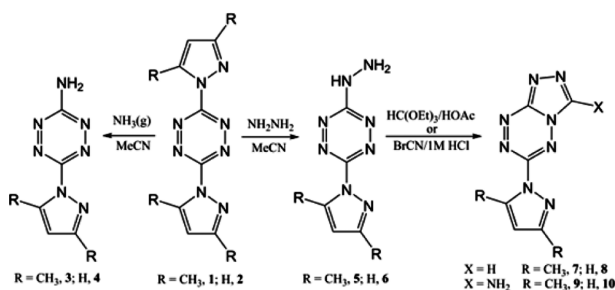
Both ring systems had been previously synthesized with dimethylpyrazole groups (3, 7, and 9), but to reduce the carbon content of these ligands, we also prepared the pyrazole systems (4, 8, and 10) by analogous routes.

We utilized perchlorate counterions to improve the oxygen balance further in the resulting complexes. The reaction of 3 or 4 with [Fe(H$_2$O)$_6$][ClO$_4$]$_2$ proceeded rapidly to form air-stable dark-blue [(NH$_2$TzDMP)$_3$Fe][ClO$_4$]$_2$ (11) and dark-purple [(NH$_2$TzPyr)$_3$Fe][ClO$_4$]$_2$ (12) in 78 and 83% isolated yield, respectively (Scheme 2). Single-crystal X-ray crystallography

Scheme 2. Synthesis of 11 and 12 from 3 and 4
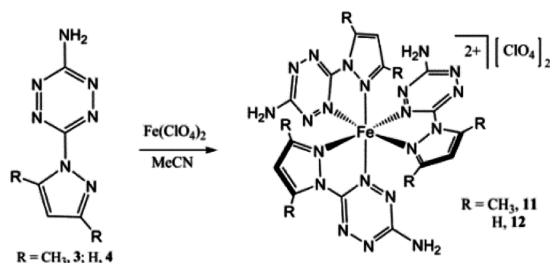
confirmed the geometry of 11 and 12 as distorted octahedral complexes with three coordinated tetrazine ligands (Figure 1).

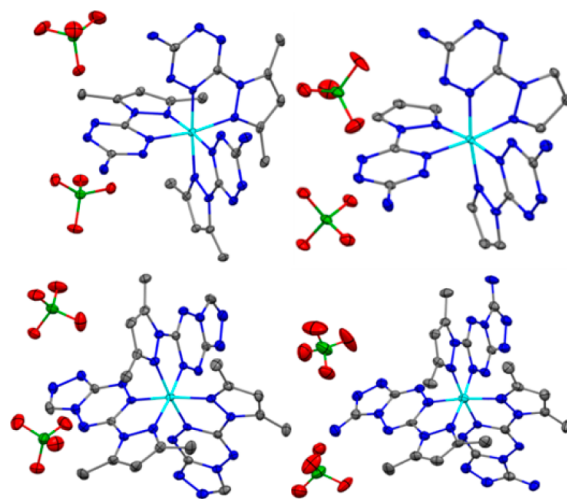**Figure 1.** X-ray crystal structures of [(NH$_2$TzDMP)$_3$Fe][ClO$_4$]$_2$ in 11 (top left) and [(NH$_2$TzPyr)$_3$Fe][ClO$_4$]$_2$ in 12 (top right). [(TriTzDMP)$_3$Fe][ClO$_4$]$_2$ in 13 (bottom left) and [(NH$_2$TriTzPyr)$_3$Fe][ClO$_4$]$_2$ in 15 (bottom right). Cyan, green, red, blue, and gray ellipsoids represent Fe, Cl, O, N, and C atoms, respectively. Ellipsoids are at 40% probability. H atoms and solvent molecules are omitted for clarity.

Complex 11 is isostructural with the previously reported NO$_3^-$ and BF$_4^-$ complex derivatives.[13] The bond lengths and angles in 12 are largely consistent with those in 11, with a few notable exceptions. The N$_{Pyr}$−N$_{Pyr}$ bond (1.378(3) Å) and the Fe−N$_{pyr}$ bond (1.978(2) Å) in 12 are both longer than those in 11 (1.365(4) Å and 1.953(6) Å). Additionally, the NH$_2$−C$_{Tz}$ bond in 12 (1.317(3) Å) is shorter than the NH$_2$−C$_{Tz}$ bond in 11 (1.328(4) Å). These differences suggest stronger σ donation from the amine group into the tetrazine ring system for 12 compared to 11.

Ligands 7−10 react with [Fe(H$_2$O)$_6$][ClO$_4$]$_2$ in MeCN to form air stable dark blue [(TriTzDMP)$_3$Fe][ClO$_4$]$_2$ (13), [(TriTzPyr)$_3$Fe][ClO$_4$]$_2$ (14), [(NH$_2$TriTzDMP)$_3$Fe][ClO$_4$]$_2$ (15) and [(NH$_2$TriTzPyr)$_3$Fe][ClO$_4$]$_2$ (16) in 81, 77, 89, and 80% yield, respectively (Scheme 3). Single-crystal X-ray crystallography confirmed the geometries of 13 and 15 (Figure 1). The lower solubility of complexes 14 and 16 resisted repeated attempts at crystallization. Both 13 and 15 are distorted octahedral complexes with three tetrazine ligands. The Fe−N$_{Tz}$ bond in 11 (1.907(6) Å) is comparable to the bonds in 13 (1.911(3) Å) and in 15 (1.894(5) Å). The Fe−

Scheme 3. Synthesis of 13−16 from 7−10
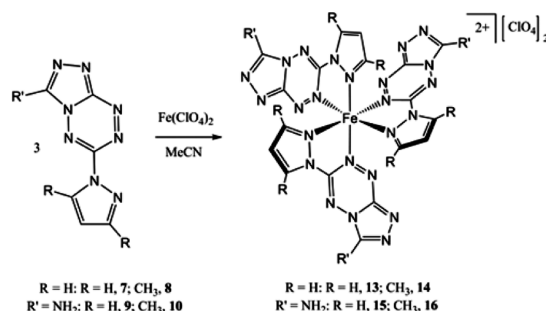
N_{Pyr} bond in **11** (1.953(6) Å is shorter than the bond in **13** (1.980(3) Å) and similar to the bond in **15** (1.959(5) Å). Unlike **11**, which has similar N_{Tz}–N_{Tz} bond lengths (1.318(4) and 1.318(4) Å), complexes **13** and **15** each have one short (1.307(3) and 1.311(5) Å, respectively) and one long (1.358(3) and 1.358(5) Å, respectively) N_{Tz}–N_{Tz} bond. This is due to the loss of double bond delocalization imposed by the fused ring system.

Structure optimizations (B3LYP/6-31G*) of **11**–**13** and **15** are in good agreement with values from the experimental crystal structures (Table S3).

Electrochemical Properties. The electrochemistry of MLCT complexes often correlates with the energy of the associated transitions. Thus, the electrochemical behavior of the ligands and their resulting Fe(II) complexes was investigated by cyclic voltammetry (Figures 2 and 3 and Tables 1 and 2). Each
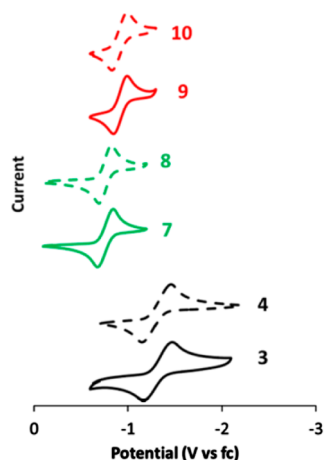

Figure 2. Cyclic voltammagrams of **3** (black, solid), **4** (black, dashed), **7** (green, solid), **8** (green, dashed), **9** (red, solid), and **10** (red, dashed). Measurements recorded in 0.1 M Bu$_4$NPF$_6$ DMSO solutions with 2.0 mM sample at 200 mV/s scan rate.
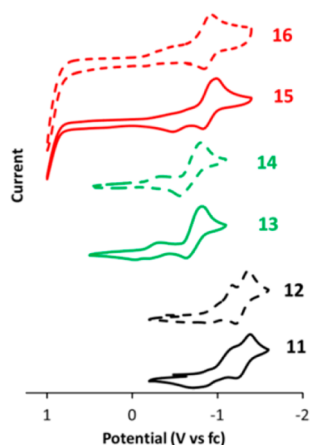

Figure 3. Cyclic voltammagrams of **11** (black, solid), **12** (black, dashed), **13** (green, solid), **14** (green, dashed), **15** (red, solid), and **16** (red, dashed). Measurements recorded in 0.1 M Bu$_4$NPF$_6$ DMSO solutions with 2.0 mM sample at 200 mV/s scan rate.

ligand displayed a single reversible reduction event corresponding to the formation of the tetrazine radical anion. Ligands **7** and **8** were reduced at the mildest potentials, whereas ligands **3** and **4** were reduced at the most negative potentials, indicating that **7** and **8** had the lowest energy $\pi*$ systems whereas **3** and **4**

Table 1. Redox Events in 3, 4, and 7−10

	$\Delta E_{1/2}$
3	−1.31
4	−1.29
7	−0.77
8	−0.75
9	−0.90
10	−0.90

Table 2. Redox Events in 11−16

	ΔE_{pc}		ΔE_{pa}
11	−1.15	−1.38	
12	−1.16	−1.35	
13	−0.31	−0.81	
14	−0.30	−0.80	
15	−0.61	−1.00	0.83
16	−0.46	−0.91	0.80

had the highest energy $\pi*$ systems. This ordering is because **7**−**10** have expanded π systems that are more readily reduced whereas **9** and **10** each have an additional σ-donating NH$_2$ group which makes **9** and **10** more difficult to reduce than **7** or **8** but easier to reduce than **3** or **4**.

The electrochemistry of the metal complexes was more complicated. Each complex showed multiple irreversible reductions corresponding to successive reductions of the tetrazine ligands. There is separation between the reduction of the first and second tetrazine ligand for each complex, but the reduction of the second and third tetrazine ligand appear to overlap for each complex. The expanded tetrazine ring systems in **15** and **16** have tetrazine reductions that are on average 510 mV more anodic than the tetrazine reductions in **11** and **12**. Complexes **13** and **14** have tetrazine reductions that are on average an additional 700 mV more anodic compared to those in **11** and **12**. The Fe^{II}/Fe^{III} redox couple is within the DMSO solvent window for **15** and **16** but not for **11**−**14**. Overall, the ligand-based reductions in **11**−**16** match the trend observed for the free ligands, and the cathodic shifts in the Fe^{II}/Fe^{III} couple in **15** and **16** are consistent with σ donation from the NH$_2$ group on the Tz ligand.

Simulated ionization potentials and electron affinities match the trends observed in the electrochemistry of **11**−**16** (Table 3). Although the Fe^{II}/Fe^{III} oxidation is not directly observed in

Table 3. Calculated Electron Affinity and Ionization Potentials of 11−16

	EA (eV)	IP (eV)
11		−6.50
12		−6.26
13	−4.71	−6.78
14	−4.61	−6.56
15	−4.37	−6.23
16	−−4.29	−6.05

11 and **13**, calculated values suggest that **11** should be oxidized at a milder potential than **13**, likely due to the presence of the electron-donating NH$_2$ group in **13**.

Optical Properties. The UV−vis spectra of **11**−**16** were collected in the solid state as KBr pellets. Because of solubility constraints, only complexes **11**, **13**, and **15** were collected in acetone solution (Figures 4 and 5). In solution, complexes **11**,
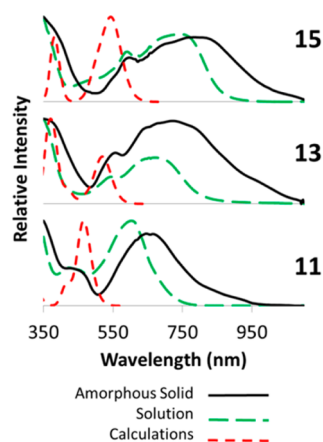
Figure 4. Linear absorption spectra of **11** (bottom), **13** (middle), and **15** (top) as an amorphous solid in KBr (black solid), in acetone solution (green long dashed), and TD-DFT calculations (red dashed).
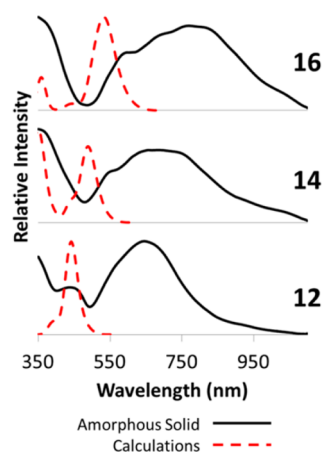

Figure 5. Linear absorption spectra of **12** (bottom), **14** (middle), and **16** (top) as an amorphous solid in KBr (black solid) and TD-DFT calculations (red dashed).

13, and **15** each displayed several ligand-based absorbances from 250 to 500 nm along with intense MLCT bands. The MLCT band in **11** is similar to those we have previously observed in Fe(II) tetrazine complexes.[13] The MLCT band in the solution spectra of **13** has a bathochromic shift relative to **11**. This is likely due to the lower energy π^* system in ligand **7** caused by the expansion of the tetrazine ring system. In solution, complex **15** has a MLCT band that has a bathochromic shift relative to both **11** and **13**. Although the energy of π^* system in ligand **9** lies between that of **3** and **7**, donation from the NH_2 group destabilizes the energy of the Fe d orbitals leading to the overall lowest energy transitions.

The solid-state spectra of **11**−**16** showed the same trend observed in the solution state with **11** having the highest energy MLCT band and **15** having the lower energy MLCT band. However, there were significant differences between the solid and solution state measurements. The absorptions in the spectra of the amorphous solid were much broader and had a bathochromic shift and a low-energy tail extending well into the near-infrared region of the spectra. We attribute these effects to the intermolecular interactions present in solids and to intramolecular conformational disorder.

The most practical wavelength for laser initiation is 1064 nm because of the availability of high power Nd:YAG lasers. The

tuning of the MLCT bands to lower energy in **13**−**16** led to significant absorption at 1064 nm in the solid state, whereas complexes **11** and **12** have negligible absorbance at that wavelength (Table 4). Overall, the pyrazole derivatives absorb

Table 4. Relative Intensity of the Absorption at 1064 nm in the Solid-State UV−Vis−NIR Spectra of 11−16

	relative intensity (1064 nm)
11	0.004
12	0.007
13	0.064
14	0.075
15	0.074
16	0.106

slightly more 1064 nm light than the corresponding dimethylpyrazole derivatives, which is consistent with their electrochemical behavior.

The nature of the transitions in **11**−**16** was investigated further with TDDFT calculations. The relative ordering of the charge transfer bands in **11**, **13**, and **15** were reproduced along with reasonable agreement in the relative intensities of the various bands when compared to the solution spectra (Table S3). We observe systematic blueshifts of about 0.5 eV pronounced for calculated MLCT transitions. The natural transition orbitals (NTOs) for the lowest energy transition reveal significant MLCT and interligand charge transfer (ILCT) character typical of d^6 metal complexes (Figures 6
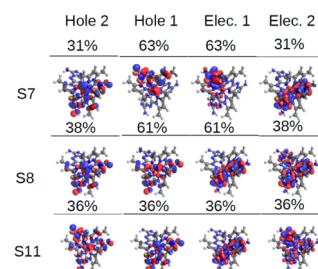

Figure 6. Dominant natural transition orbital pairs for the first three excited states (S7, S8, and S11) of **15**. Contributing holes for each state on the left and contributing particles on the right.

and S1).[14] Notably, all NTOs show predominantly multi-configurational character such that each transition can be adequately described by two distinct pairs of transition orbitals. Of particular interest are the NTOs for complex **15**, which show significant contribution from the amine groups, corroborating the observed accessible Fe^{II}/Fe^{III} oxidation and lower energy charge transfer band.

The successful reproduction of the observed experimental trends and electronic nature of the transitions indicates that it is possible to predict the linear optical response in metal tetrazines. This capability should allow for the design of new systems with even greater absorption of NIR light.

Explosive Properties. The thermal stability of each complex was examined through differential scanning calorimetry (DSC) (Figures S2−S7 and Table 5). Each complex has a broad exothermic feature with an onset temperature between 169.2 and 207.6 °C that peaked between 222.9 and 254.4 °C. The sensitivity of the pyrazole derivatives **12**, **14**, and **16** toward mechanical stimuli and electrostatic discharge (ESD)

Table 5. Decomposition Temperatures, Densities, Oxygen Balances, and Nitrogen Percentages of 11−16

	T_0 (°C)[a]	ρ (g/cm^3)[b]	Ω[c]	%N
11	169.2	1.595[d]	−91.8%	35.51%
12	207.6	1.633[d]	−63.5%	39.24%
13	185.1	1.661[d]	−92.2%	37.08%
14	180.0		−66.4%	41.04%
15	189.1	1.507[e]	−90.3%	39.88%
16	178.0		−65.8%	43.76%
PETN	164.8	1.77	−10.1%	17.72%

[a]Onset of decomposition temperature. [b]X-ray crystal density. [c]Calculated oxygen balance to CO_2 Ω = −1600[2(no. of C atoms) + (no. H atoms)/2 − (no. of O atoms)]/MW; [d]MeCN adduct. [e]DMF adduct.

was investigated quantitatively (Table 6). All three compounds have sensitivity toward ESD that was similar to that of PETN,

Table 6. Mechanical Sensitivity Properties of 12, 14, and 16

	impact (J)[a]	friction (N)[b]	ESD (J)[c]	laser initiation[d]
12	4.2 ± 0.7	78 ± 9	0.0625[e]	−
14	8.5 ± 2.8	183 ± 27	0.0625[e]	+
16	12.4 ± 2.6	195 ± 26	0.0625	+
PETN	2.9 ± 0.6	78 ± 22	0.0625[e]	−

[a]LANL type 12, 50% drop height, 2.5 kg. [b]BAM 50% load. [c]ABL spark 3.4% threshold initiation level (TIL). [d]Initiation during irradiation with a 10 ns, 35 mJ pulse from a Nd:YAG laser. [e]Compounds 12, 14, and **PETN** had ESD thresholds of 0.025 J during certain days of testing.

likely due to the presence of the perchlorate counteranion. Compound **12** has similar impact and friction sensitivities compared to PETN, whereas compounds **14** and **16** are significantly less sensitive. This difference may be related to an increase in stability of the fused ring systems in **14** and **16** and the higher nitrogen content of those materials relative to **12**. Overall, the complexes are all considered secondary explosives.

Complexes **12**, **14**, and **16** along with PETN were subjected to laser initiation tests. A confined 50 mg sample of each compound was irradiated with a 35 mJ 10 ns pulse of 1064 nm light through a 1 mm optical fiber. The energy density achieved in this configuration (4.5 J/cm^2) is lower than the reported threshold for confined low density PETN at 1064 nm (6.4 J/cm^2).[6] Notably, both **14** and **16** could be initiated under these conditions but **12** and PETN failed to initiate. In the solid state, both **14** and **16** have significant absorption at 1064 nm, whereas **12** and PETN do not, which accounts for their different behavior under irradiation. Although this threshold is not quite as low as the threshold for PETN at UV wavelengths or that of PETN doped with nonexplosive absorbant materials, the drammatic improvement in mechanical sensitivity for these new complexes compared to that of PETN is remarkable. Complexes **14** and **16** are the first reported materials that are both safer and more reliable than pure PETN for initiation with practical NIR lasers.

■ CONCLUSIONS

We have synthesized the air-stable complexes [(NH$_2$TzDMP)$_3$Fe][ClO$_4$]$_2$ (**11**), [(NH$_2$TzPyr)$_3$Fe][ClO$_4$]$_2$ (**12**), [(TriTzDMP)$_3$Fe][ClO$_4$]$_2$ (**13**), [(TriTzPyr)$_3$Fe]-[ClO$_4$]$_2$ (**14**), [(NH$_2$TriTzDMP)$_3$Fe][ClO$_4$]$_2$ (**15**), and

[(NH$_2$TriTzPyr)$_3$Fe][ClO$_4$]$_2$ (**16**), which are all secondary explosives with strong MLCT transitions in the visible and NIR regions of the spectrum. Rational design of the ligand architecture allowed us to tune the MLCT band from the visible region of the spectrum for **11** and **12** to the near-infrared region of the spectrum for **13−16**. This control of the optical properties was critical to the successful laser initiation of these complexes. Complexes **14** and **16** were initiated with 1064 nm light from a Nd:YAG laser at an energy density of 4.5 J/cm^2, which is significantly lower than the threshold for pure PETN (6.4 J/cm^2). Furthermore, complexes **14** and **16** are substantially less sensitive than PETN toward mechanical stimuli (e.g., impact and friction). Our TD-DFT results compare well with experiment and further our understanding of the electronic properties in these new explosive metal tetrazine systems. Together, these results provide the foundation necessary to design future secondary explosive systems with increased absorption of NIR light and subsequent reduction of the laser initiation threshold. Complexes **14** and **16** are the first explosives that are both safer to handle and easier to initiate with NIR lasers than PETN and are being pursued for laser initiation applications.

■ EXPERIMENTAL SECTION

*Caution! Although no problems have occurred during the synthesis and handling of these materials, complexes **11−16** are explosive. Laboratories and personnel should be properly grounded and safety equipment such as Kevlar gloves, blast shields, and ear plugs are necessary, especially when working with large-scale reactions.*

Physical Measurements. Elemental analyses for **6**, **8**, and **10** were carried out by Atlantic Microlab, Inc. of Norcross, GA. Elemental analyses for all other complexes were carried out in house using a PerkinElmer series II 2400 CHNS/O analyzer. Elemental analysis of explosive compounds often returns low values for the %N, and materials were purified until satisfactory %C and %H values were obtained.[15] ^{1}H NMR spectra were recorded at ambient temperature using a Bruker Avance 400 MHz spectrometer. Chemical shifts (δ) were referenced to the residual solvent signal. Electrochemical measurements were recorded under a dinitrogen atmosphere using a CHI Electrochemical Analyzer, a glassy carbon working electrode, a Pt wire auxiliary electrode, and a Ag/AgNO$_3$ nonaqueous reference electrode. Reported potentials are all referenced to the Fc/Fc$^+$ couple and were determined using ferrocene as an internal standard. UV−vis spectra were recorded in acetone solutions or as KBr pellets using an HP 8453 Agilent UV−vis spectrometer.

X-ray Structure Determinations. X-ray diffraction studies were carried out on a Bruker APEX II equipped with a CCD area detector. Measurements were carried out at −173 °C using Mo Kα 0.71073 radiation. Crystals were mounted on a Kaptan loop with paratone-*N* oil. Initial lattice parameters were obtained from a least-squared analysis of more than 100 centered reflections; these parameters were later refined against all data. Data were integrated and corrected for Lorentz polarization effects using SAINT[16] and were corrected for absorption effects using SADABS 2.3.[17]

Space group assignments were based upon systematic absences, *E* statistics, and successful refinement of the structures. Structures were solved by direct methods with the aid of successive difference Fourier maps and were refined against all data using the SHELXTL 5.0 software package.[18] Thermal parameters for all nonhydrogen atoms were refined anisotropically. Hydrogen atoms, where added, were assigned to ideal positions and refined using a riding model with an isotropic thermal parameter 1.2 times that of the attached carbon atom (1.5 times for methyl hydrogens).

Computational Methods. Simulations were carried out using the density functional theory (DFT) and time-dependent DFT (TD-DFT) in Gaussian 09.[19] All calculations were carried out with the B3LYP functional.[20] The 6-31G* basis set was chosen for first row

elements, whereas for Fe, the 6-31G* basis is used for valence electrons and LANL2DZ pseudopotential for core electrons.[21,22] Optimized geometries were found to be comparable to experimental crystal structures, with Fe−N bond lengths overestimated by approximately 0.05 Å (Table 1).

Prediction of the optical properties of these molecules was carried out with TD-DFT. Several functionals were compared with experimental absorption spectra. To include the effects of a dielectric environment, the polarizable continuum model (PCM) was used.[23] In calculations of the absorption spectra, PCM was used in the linear response formalism.[24−26]

The ionization potential (IP) and electron affinity (EA) were simulated using the optimized ground-state geometries calculated with the PCM solvent model parametrized for DMSO. We neglect the zero-point vibrational energy and calculate the EA and IP from

$$EA = E(-1) - E(0) \quad (2a)$$

$$IP = E(0) - E(+1) \quad (2b)$$

where $E(n)$ is the energy of the molecule with n change in its charge (0 corresponds to a charge of +2 for coordination compounds).[27]

Laser Initiation Experiments. The sample holder was composed of a 1/2 in. thick aluminum plate bolted to a 1/2 in. thick copper plate. The aluminum plate had 1/8 in. diameter holes drilled through so that the final cavity was 1/2 in. deep with a diameter of 1/8 in. The 50 mg sample was loaded as a loose powder into the cavity, and the 1 mm diameter optical fiber was inserted on top of the sample. To seal the cavity and confine the sample, the optical fiber was secured and sealed in place with epoxy. The diameter casing around the fiber was 1/8 in., and the fiber extended 1/4 in. into the cavity confining the sample to a 1/4 in. deep by 1/8 in. volume for an approximate density of 1 g/cm³. The sample holder was placed inside of a box made from 1 in. thick steel with the fibers threaded out through a 1 in. diameter hole on one side. A Quantel Big Sky Laser Ultra/CFR 1064 nm 50 mJ was used to supply the 10 ns pulse to the sample (laser power = 5 MW). Measurements showed that the average power delivered through the fiber was 35 mJ. The samples were irradiated with a single pulse with initiation determined through an audible reaction and examination of the aluminum copper plates after disassembly.

Preparation of Compounds. Deuterated solvents were purchased from Cambridge Isotopes Laboratories, Inc. and used without purification. The compounds bis-3,6-(3,5-dimethylpyrazolyl)1,2,4,5-tetrazine (DMP₂Tz, **1**), bis-3,6-(pyrazolyl)1,2,4,5-tetrazine (Pyr₂Tz, **2**), 3-amino-6-(3,5-diemthylpyrazolyl)-1,2,4,5-tetrazine (NH₂TzDMP, **3**), 3-amino-6-(pyrazolyl)-1,2,4,5-tetrazine (NH₂TzPyr, **4**), 3-hydrazi-no-6-(3,5-dimethylpyrazolyl)-1,2,4,5-tetrazine (NH₂NHTzDMP, **5**), 6-(3,5-dimethylpyrazol-1-yl)-1,2,4-triazolo[4,3-b][1,2,4,5]tetrazine (TriTzDMP, **7**), 3-amino-6-(3,5-dimethylpyrazol-1-yl)-1,2,4-triazolo-[4,3-b][1,2,4,5]tetrazine (NH₂TriTzDMP, **9**) were synthesized according to literature procedures.[28] All other reagents were purchased from commercial vendors and used without purification.

NH₂NHTzPyr (6). Hydrazine hydrate (0.500 g, 10.0 mmol) was added dropwise to a stirred solution of **2** (2.14 g, 10.0 mmol) in MeCN (20 mL) at room temperature. The solution was heated to 70 °C for an additional 30 min. The solution was cooled to room temperature and the red-orange precipitate was collected via filtration and washed with MeCN (20 mL) to yield **6** (1.08 g, 72%) as a red-orange powder. ¹H NMR (400 MHz, d_6-DMSO, δ) 4.66 (s, 2H, NH₂), 6.66 (s, 1H, pyr-CH), 7.92 (s, 1H, pyr-CH), 8.57 (s, 1H, pyr-CH), 9.71 (s, 1H, NH). ¹³C NMR (400 MHz, d_6-DMSO, δ) 108.65 (pyr), 128.88 (pyr), 142.97 (pyr), 156.07 (tz), 163.97 (tz). Anal. Calcd for C₅H₆N₈: C, 33.74%, H, 3.40%, N, 62.95%. Found: C, 34.13%, H, 3.36%, N, 62.63%.

TriTzPyr (8). A solution of **6** (1.50 g, 10.0 mmol) and acetic acid (0.2 mL) in triethylorthoformate (5.00 mL) was heated and stirred at 100 °C for 24 h. The solution was cooled to room temperature, and the yellow precipitate was collected via filtration and washed with cold water (50 mL) and MeCN (10 mL) to yield **8** (1.63 g, 87%) as a yellow powder. ¹H NMR (400 MHz, d_6-DMSO, δ) 6.84 (s, 1H, pyr-

CH), 8.13 (s, 1H, pyr-CH), 9.03 (s, 1H, pyr-CH), 10.06 (s, 1H, triazolo-CH). ¹³C NMR (400 MHz, d_6-DMSO, δ) 110.57 (pyr), 131.81 (pyr), 137.84 (triazolo), 145.76 (pyr), 149.22 (tz), 150.81 (tz). UV−vis spectrum (KBr pellet) 256 (1.00), 363 (0.63), 434 (0.36), 472 (0.31), 541 (0.18) nm λ_{max} (relative intensity). Anal. Calcd for C₆H₄N₈: C, 38.30%, H, 2.14%, N, 59.56%. Found: C, 38.40%, H, 2.11%, N, 59.58%.

NH₂TriTzPyr (10). Cyanogen bromide (1.07 g, 10.0 mmol) was added to a stirred solution of **6** (1.50 g, 10.0 mmol) in 3 M HCl (15 mL). The solution was stirred at room temperature for 24 h. The dark-purple precipitate was collected via filtration, washed with water (50 mL) and MeCN (10 mL) to yield **10** (1.20 g, 59%) as a dark-purple powder. ¹H NMR (400 MHz, d_6-DMSO, δ) 6.76 (s, 1H, pyr-CH), 7.67 (s, 2H, NH₂), 8.03 (s, 1H, pyr-CH), 8.87 (s, 1H, pyr-CH). ¹³C NMR (400 MHz, d_6-DMSO, δ) 109.70(pyr), 131.29 (pyr), 144.66 (pyr), 148.11 (tz), 149.46 (tz), 149.71 (triazolo). UV−vis spectrum (KBr pellet) 244 (1.00), 286 (0.99), 386 (0.44), 543(0.20) λ_{max} (relative intensity). Anal. Calcd for C₆H₅N₉: C, 35.50%, H, 2.48%, N, 62.10%. Found: C, 35.47%, H, 2.53%, N, 61.12%.

[(NH₂TzDMP)₃Fe][ClO₄]₂ (11). A solution of **3** (1.92 g, 10.0 mmol) in MeCN (5 mL) was added to a stirred solution of [Fe(H₂O)₆]-[ClO₄]₂ (1.21 g, 3.33 mmol) in MeCN (10 mL). The solution was stirred for 15 min until it was a uniform blue color. Diethyl ether (10 mL) was added, and **11** (2.10 g, 78%) was collected as a dark-blue solid via filtration. Single crystals of **11** were grown from a concentrated MeCN solution at 0 °C over 3 days. ¹H NMR (400 MHz, d_6-DMSO, δ) 8.02 (s, 1H, NH₂), 6.09 (s, 1H, Pyr-H), 2.05 (s, 3H, CH₃), 1.83 (s, 3H, CH₃). UV−vis spectrum (KBr pellet) 288 (1.00), 351 (0.70), 459 (0.57), 651 (0.94) λ_{max} (relative intensity). UV−vis spectrum (acetone) 337 (17 200), 420 (7750), 458 (7360), 605 (17 400) λ_{max} (ε). Anal. Calcd for C₂₁H₂₇Cl₂FeN₂₁O₈: C, 30.45%, H, 3.29%, N, 35.15%. Found: C, 30.60%, H, 3.16%, N, 34.42%.

[(NH₂TzPyr)₃Fe][ClO₄]₂ (12). A suspension of **4** (1.63 g, 10.0 mmol) in MeCN (5 mL) was added to a stirred solution of [Fe(H₂O)₆]-[ClO₄]₂ (1.21 g, 3.33 mmol) in MeCN (5 mL). The solution was stirred for 15 min until it was a uniform violet color. Diethyl ether (10 mL) was added, and **12** (2.06 g, 83%) was collected as a dark-blue solid via filtration. Single crystals of **12** were grown from the diffusion of diethyl ether into a concentrated MeCN solution over 2 days. ¹H NMR (400 MHz, d_6-DMSO, δ) 8.47 (s, 1H, Pyr-H), 7.96 (s, 1H, Pyr-H), 7.78 (s, 1H, NH₂), 6.70 (s, 1H, Pyr-H). UV−vis spectrum (KBr pellet) 284 (1.00), 345 (0.63), 448 (0.38), 560 (0.59), 639 (0.77) λ_{max} (relative intensity). Anal. Calcd for C₁₅H₁₅Cl₂FeN₂₁O₈·C₂H₃N: C, 26.00%, H, 2.31%, N, 39.24%. Found: C, 25.99%, H, 2.29%, N, 39.38%.

[(TriTzDMP)₃Fe][ClO₄]₂ (13). A solution of **7** (2.16 g, 10.0 mmol) in MeCN (5 mL) was added to a stirred solution of [Fe(H₂O)₆][ClO₄]₂ (1.21 g, 3.33 mmol) in MeCN (5 mL). The solution was stirred for 15 min until it was a uniform blue color. Diethyl ether (10 mL) was added, and **13** (2.43 g, 81%) was collected as a dark-blue solid via filtration. Single crystals of **13** were grown from layering a solution containing 3 mmol of **7** in MeCN (10 mL) over a solution containing 1 mmol of [Fe(H₂O)₆][ClO₄]₂ in MeCN (10 mL) and leaving the resulting solution undisturbed for 1 week. ¹H NMR (400 MHz, d_6-DMSO, δ) 2.18 (s, 3H, CH₃), 2.51 (s, 3H, CH₃), 6.27 (s, 1H, pyr-CH), 9.94 (s, 1H, triazolo-CH). UV−vis spectrum (KBr pellet) 269 (1.00), 368 (0.55), 550 (0.30), 646 (0.50), 741 (0.53) λ_{max} (relative intensity). UV−vis spectrum (acetone) 339 (30 100), 543 (9210), 676 (br, 15 600) λ_{max} (ε). Anal. Calcd for C₂₄H₂₄Cl₂FeN₂₄O₈·C₂H₃N: C, 33.06%, H, 2.88%, N, 37.08%. Found: C, 33.17%, H, 2.97%, N, 37.01%.

[(TriTzPyr)₃Fe][ClO₄]₂ (14). A suspension of **8** (1.88 g, 10.0 mmol) in MeCN (5 mL) was added to a stirred solution of [Fe(H₂O)₆]-[ClO₄]₂ (1.21 g, 3.33 mmol) in MeCN (5 mL). The solution was stirred for 15 min until it was a uniform blue color. Diethyl ether (10 mL) was added, and **14** (2.10 g, 77%) was collected as a dark-blue solid via filtration. ¹H NMR (400 MHz, d_6-DMSO, δ) 6.73 (s, 1H, pyr-CH), 8.02 (s, 1H, pyr-CH), 8.92 (s, 1H, pyr-CH), 9.98 (s, 1H, triazolo-CH). UV−vis spectrum (KBr pellet) 265 (1.00), 355 (0.69), 540 (0.45), 633 (0.62), 708 (0.62) λ_{max} (relative intensity). Anal. Calcd

for $C_{18}H_{12}Cl_2FeN_{24}O_8$: C, 26.39%, H, 1.48%, N, 41.04%. Found: C, 26.60%, H, 1.55%, N, 41.34%.

[(NH₂TriTzDMP)₃Fe][ClO₄]₂ (15). A solution of **9** (2.31 g, 10.0 mmol) in MeCN (5 mL) was added to a stirred solution of [Fe(H₂O)₆][ClO₄]₂ (1.21 g, 3.33 mmol) in MeCN (5 mL). The solution was stirred for 15 min until it was a uniform blue color. Diethyl ether (10 mL) was added, and **15** (2.81 g, 89%) was collected as a dark-blue solid via filtration. Single crystals of **15** were grown from the slow diffusion of diethyl ether into a concentrated DMF solution at 0 °C over 4 days. ¹H NMR (400 MHz, d_6-DMSO, δ) 2.10 (s, 3H, CH₃), 2.43 (s, 3H, CH₃), 6.15 (s, 1H, pyr-CH), 7.74 (s, 2H, NH₂). UV–vis spectrum (KBr pellet) 243 (1.00), 288 (0.98), 343 (0.64), 592 (0.44), 693 (0.53), 752 (0.55), 822 (0.56), 1010 (0.19) λ_{max} (relative intensity). UV–vis spectrum (acetone) 338 (24 000), 585 (13 200), 689 (br, 16 600), 757 (br, 17 800) λ_{max}. Anal. Calcd for $C_{24}H_{27}Cl_2FeN_{27}O_8$: C, 30.39%, H, 2.87%, N, 39.88%. Found: C, 30.35%, H, 2.92%, N, 40.19%.

[(NH₂TriTzPyr)₃Fe][ClO₄]₂ (16). A solution of **10** (2.03 g, 10.0 mmol) in MeCN (5 mL) was added to a stirred solution of [Fe(H₂O)₆][ClO₄]₂ (1.21 g, 10.0 mmol) in MeCN (5 mL). The solution was stirred for 15 min until it was a uniform blue color. Diethyl ether (10 mL) was added, and **16** (2.30 g, 80%) was collected as a dark-blue solid via filtration. ¹H NMR (400 MHz, d_6-DMSO, δ) 6.69 (s, 1H, pyr-CH), 7.57 (s, 2H, NH₂), 7.96 (s, 1H, pyr-CH), 8.79 (s, 1H, pyr-CH). UV–vis spectrum (KBr pellet) 283 (1.00), 366 (0.73), 566 (0.39), 674 (0.45), 752 (0.46), 828 (0.37), 922 (0.18) λ_{max} (relative intensity). Anal. Calcd for $C_{18}H_{15}Cl_2FeN_{27}O_8$: C, 25.01%, H, 1.75%, N, 43.76%. Found: C, 25.24%, H, 1.97%, N, 43.61%.

ASSOCIATED CONTENT

ⓢ Supporting Information

The Supporting Information is available free of charge on the ACS Publications website at DOI: 10.1021/jacs.6b02155.

> Crystallographic data, DSC plots, and additional NTOs. (PDF)
> Crystallographic information files: TWM1 in the CIF file corresponds to compound **13** in the paper; TWM2 in the CIF file corresponds to compound **12** in the paper; TWM3 in the CIF file corresponds to compound **11** in the paper; TWM4 in the CIF file corresponds to compound **15** in the paper. (CIF)

AUTHOR INFORMATION

Corresponding Author

*twmyers@lanl.gov

Notes

The authors declare no competing financial interest.

ACKNOWLEDGMENTS

REFERENCES

(1) Ahmad, S. R.; Cartwright, M. In *Laser Ignition of Energetic Materials*; Wiley-VCH: Weinheim, 2015; pp 17−33.

(2) Menichelli, V. J.; Yang, L. C. *NASA Technical Report 32−1474*; Jet Propulsion Lab., California Inst. of Tech.; Pasadena, CA, 1970.

(3) Lisitsyn, V. M.; Tsipilev, V. N.; Damamme, G.; Malis, D. *Combust., Explos. Shock Waves* **2011**, *47*, 591−600.

(4) (a) Joas, M.; Klapötke, T. M.; Szimhardt, N. *Eur. J. Inorg. Chem.* **2014**, *2014*, 493−498. (b) Fischer, N.; Joas, M.; Klapötke, T. M.; Stierstorfer, J. *Inorg. Chem.* **2013**, *52*, 13791−13802. (c) Evers, J.; Gospodinov, I.; Joas, M.; Klapötke, T. M.; Stierstorfer, J. *Inorg. Chem.* **2014**, *53*, 11749−11756. (d) Fischer, D.; Klapötke, T. M.; Piercey, D. G.; Stierstorfer, J. *J. Energ. Mater.* **2012**, *30*, 40−54. (e) Joas, M.; Klapötke, T. M. *Propellants, Explos., Pyrotech.* **2015**, *40*, 163−164.

(5) Energy density calculated from reported laser properties. Laser power density reported as on the order of 10^5 W/cm² with pulse lengths of 100 μs. For complexes with function times shorter than the pulse length, the function time was used to calculate the energy density.

(6) (a) Renlund, A. M.; Stanton, P. L.; Trott, W. M. *Proc. 9th Inter. Det. Symp.* **1989**, 1118−1127. (b) Paisley, D. L. *Proc. 9th Inter. Det. Symp.* **1989**, 1110−1117.

(7) (a) Kunz, A. B.; Kuklja, M. M.; Botcher, T. R.; Russell, T. P. *Thermochim. Acta* **2002**, *384*, 279−284. (b) Greenfield, M.; Guo, Y. W.; Bernstein, E. R. *Chem. Phys. Lett.* **2006**, *430*, 277−281. (c) Bhattacharya, A.; Bernstein, E. R. *J. Phys. Chem. A* **2011**, *115*, 4135−4147.

(8) Aduev, B. P.; Nurmukhametov, D. R.; Furega, R. I.; Zvekov, A. A.; Kalenskii, A. V. *Russ. J. Phys. Chem. B* **2013**, *7*, 453−456.

(9) Clavier, G.; Audebert, P. *Chem. Rev.* **2010**, *110*, 3299.

(10) (a) Patra, S.; Sarkar, B.; Ghumaan, S.; Patil, M. P.; Mobin, S. M.; Sunoj, R. B.; Kaim, W.; Lahiri, G. K. *Dalton Trans.* **2005**, 1188−1194. (b) Nayak, A.; Patra, S.; Sarkar, B.; Ghumaan, S.; Puranik, V. G.; Kaim, W.; Lahiri, G. K. *Polyhedron* **2005**, *24*, 333−342.

(11) (a) Chavez, D. E.; Hanson, S. K.; Veauthier, J. M.; Parrish, D. A. *Angew. Chem., Int. Ed.* **2013**, *52*, 6876−6879. (b) Chavez, D. E.; Hiskey, M. A.; Naud, D. L. *Propellants, Explos., Pyrotech.* **2004**, *29*, 209−215. (c) Chavez, D. E.; Tappan, B. C.; Hiskey, M. A.; Son, S. F.; Harry, H. H.; Montoya, D.; Hagelberg, S. *Propellants, Explos., Pyrotech.* **2005**, *30*, 412−417.

(12) (a) Benson, C. R.; Hui, A. K.; Parimal, K.; Cook, B. J.; Chen, C.-H.; Lord, R. L.; Flood, A. H.; Caulton, K. G. *Dalton Trans.* **2014**, *43*, 6513−6524. (b) Hui, A. K.; Lord, R. L.; Caulton, K. G. *Dalton Trans* **2014**, *43*, 7958−7963. (c) Ketterle, M.; Fiedler, J.; Kaim, W. *Chem. Commun.* **1998**, 1701−1702. (d) McNitt, K. A.; Parimal, K.; Share, A. I.; Fahrenbach, A. C.; Witlicki, E. H.; Pink, M.; Bediako, D. K.; Plaisier, C. L.; Le, N.; Heeringa, L. P.; Griend, D. A. V.; Flood, A. H. *J. Am. Chem. Soc.* **2009**, *131*, 1305−1313.

(13) Myers, T. W.; Chavez, D. E.; Hanson, S. K.; Scharff, R. J.; Scott, B. L.; Veauthier, J. M.; Wu, R. *Inorg. Chem.* **2015**, *54*, 8077−8086.

(14) Vlček, A., Jr.; Záliš, S. *Coord. Chem. Rev.* **2007**, *251*, 258−287.

(15) Swift, H. *Microchem. J.* **1966**, *11*, 193.

(16) *SMART Software Users Guide*, version 5.1; Bruker Analytical X-Ray Systems, Inc.; Madison, WI, 1999.

(17) *SAINT Software Users Guide*, version 7.0; Bruker Analytical X-Ray Systems, Inc.; Madison, WiI, 1999.

(18) Sheldrick, G. M. *SADABS*, version 2.03; Bruker Analytical X-Ray Systems, Inc.; Madison, WI, 2000.

(19) Frisch, M. J.; Trucks, G. W.; Schlegel, H. B.; Scuseria, G. E.; Robb, M. A.; Cheeseman, J. R.; Scalmani, G.; Barone, V.; Mennucci, B.; Petersson, G. A.; Nakatsuji, H.; Caricato, M.; Li, X.; Hratchian, H. P.; Izmaylov, A. F.; Bloino, J.; Zheng, G.; Sonnenberg, J. L.; Hada, M.; Ehara, M.; Toyota, K.; Fukuda, R.; Hasegawa, J.; Ishida, M.; Nakajima, T.; Honda, Y.; Kitao, O.; Nakai, H.; Vreven, T.; Montgomery, J. A., Jr.; Peralta, J. E.; Ogliaro, F.; Bearpark, M.; Heyd, J. J.; Brothers, E.; Kudin, K. N.; Staroverov, V. N.; Kobayashi, R.; Normand, J.; Raghavachari, K.; Rendell, A.; Burant, J. C.; Iyengar, S. S.; Tomasi, J.; Cossi, M.; Rega, N.; Millam, J. M.; Klene, M.; Knox, J. E.; Cross, J. B.; Bakken, V.; Adamo, C.; Jaramillo, J.; Gomperts, R.; Stratmann, R. E.; Yazyev, O.;

Austin, A. J.; Cammi, R.; Pomelli, C.; Ochterski, J. W.; Martin, R. L.; Morokuma, K.; Zakrzewski, V. G.; Voth, G. A.; Salvador, P.; Dannenberg, J. J.; Dapprich, S.; Daniels, A. D.; Farkas, O.; Foresman, J. B.; Ortiz, J. V.; Cioslowski, J.; Fox, D. J. *Gaussian 09*, revision D.02; Gaussian, Inc.: Wallingford, CT, 2009.

(20) Becke, A. D. *J. Chem. Phys.* **1993**, *98*, 5648−5652.

(21) Pople, J. A.; Gill, P. M. W.; Johnson, B. G. *Chem. Phys. Lett.* **1992**, *199*, 557−560.

(22) Hay, P. J.; Wadt, W. R. *J. Chem. Phys.* **1985**, *82*, 299−310.

(23) Mennucci, B. *Wiley Interdiscip. Rev. Comput. Mol. Sci.* **2012**, *2*, 386−404.

(24) Scalmani, G.; Frisch, M. J.; Mennucci, B.; Tomasi, J.; Cammi, R.; Barone, V. *J. Chem. Phys.* **2006**, *124*, 094107.

(25) Martin, R. L. *J. Chem. Phys.* **2003**, *118*, 4775−4777.

(26) Hanwell, M. D.; Curtis, D. E.; Lonie, D. C.; Vandermeersch, T.; Zurek, E.; Hutchison, G. R. *J. Cheminf.* **2012**, *4*, 17.

(27) Zhan, C.-G.; Nichols, J. A.; Dixon, D. A. *J. Phys. Chem. A* **2003**, *107*, 4184−4195.

(28) (a) Chavez, D. E.; Hiskey, M. A. *J. Heterocycl. Chem.* **1998**, *35*, 1329−1332. (b) Wei, H.; Gao, H.; Shreeve, J. M. *Chem. - Eur. J.* **2014**, *20*, 16943−16952. (c) Klapötke, T. M.; Preimesser, A.; Stierstorfer, J. *Z. Naturforsch., B: J. Chem. Sci.* **2013**, *68*, 1310−1320.